3rd Automotive Steel International Conference
9–12 March 2025, Orlando, Fla., USA
10.33313/200/003

Investigating the Microstructures and Mechanical Properties of As-Cast and Continuously Cast Advanced High-Strength Steels

Nhu Nguyen Anh Ngo[1], Bryan Webler[1], P. Chris Pistorius[1], Thinium Natarajan[2]

[1]Carnegie Mellon University
5000 Forbes Avenue, Pittsburgh PA 15213
Phone: 857-869-4982
Email: nnngo@andrew.cmu.edu

[2]U.S Steel Research and Technology Center
800 E Waterfront Dr, Munhall, PA 15120

Keywords: AHSS, microstructure, continuously cast, ingots, slabs

ABSTRACT

Third-generation advanced high-strength steels (AHSS) exhibit increased strength and formability due to their chemical composition and precisely controlled thermomechanical processing. Reliable production of these steels requires understanding of the chemical composition effects on microstructure development during all steps of processing. This study focuses on comparing laboratory-cast ingots with continuously casted slabs containing 0.2 wt.% C, with varying Mn, Si and Al concentrations. Microstructural features and mechanical properties are investigated throughout the study. Results show that higher alloying addition increases the A_3 transformation temperature and amount of ferrite. For as-cast microstructures, Si-containing steels have proeutectoid ferrite while the combined Si and Al alloys have primary ferrite. Steels alloyed with only Al have both primary and proeutectoid ferrite. Gleeble results show that ferrite does not affect the fracture path for all compositions.

INTRODUCTION

Over the past decades, developing lighter and stronger steels for automotive applications has been a priority in the steel industry. The result of this extensive research is the emergence of higher-strength steels known as advanced high-strength steels (AHSSs) which improve fuel-efficiency, passenger safety and emissions while being cost-effective for manufacturing purposes[1]. The goals for developing these steels are to increase the yield strength, improve formability and ensure compatibility for other manufacturing processes such as forming, painting, coating and assembly[2].

Common chemical compositions of 3rd generation AHSSs include 0.06-0.2% carbon (C), 1.5-5.0% manganese (Mn), 0.2-3.0% silicon (Si) and/or 0.04-3.0% aluminum (Al)[1,3]. Chemical compositions affect the microstructure of these steels. With the nature of the continuous casting and cooling process, the microstructure can be complicated which can potentially influence the cracking behavior in these steels.

For the purpose of this paper, the three main microstructures that will be focused on are ferrite, pearlite and bainite. While there are various types of ferrites, the two main types discussed throughout are primary and proeutectoid ferrite. Proeutectoid ferrite grows along the austenite grain boundaries during the austenite to ferrite transformation. Primary ferrite has two forms – delta (δ) and alpha (α). α ferrite is identical to δ ferrite. It was known prior that the proeutectoid formation is usually seen in most microstructures, the question of whether retention of primary ferrite would be possible given the difference in the alloy compositions remains. Primary ferrite grows dendritically during solidification with both the main trunk and side-arms growing in the <100> direction. Upon further cooling, some of this ferrite can transform to austenite with ferrite subsequently regrowing from the dendrite remnants once the austenite-ferrite transformation starts before the eutectoid reaction.

It is not fully understood why these steels crack while cooling. Hence, it is necessary to investigate further the cracking mechanisms that happen upon cooling of AHSSs slabs after casting typically at temperatures from 100ºC to 300ºC. It is also currently unclear whether the main cracking mechanisms of these slabs are associated with the microstructures, processing

© 2025 by the Association for Iron & Steel Technology.

procedures, pre-existing defects or stresses that are applied to the slab during cooling or handling so investigating into the different factors that can influence will help to determine the cracking mechanisms.

There are two types of fracture – brittle and ductile. Brittle fracture consists of both cleavage and intergranular fracture. Cleavage fracture typically follows cleavage planes which are the {100} planes for ferritic steels. Common features of brittle fracture include steps or ridges that appear on the surface[6]. Cleavage fracture dictates the toughness in the lower shelf temperature. Ductile fracture is the most common failure mechanism in metals. The mechanisms of ductile fracture are governed nucleation, growth and coalescence of voids. In high strength alloys, this process occurs rapidly which results in very low ductility for some cases[6,7].

Void formation or nucleation typically occurs at second-phase particles which are usually inclusions. In materials with a hard/soft matrix, nucleation is governed by particle decohesion. In hard matrices, particle cracking is preferred, and this mechanism is explored above in cleavage fracture. A softer matrix would arrest the particle stress to reach the critical stress for the particles to crack while the buildup of plastic strain in the particle/matrix interface allows for opening of defects[6, 7].

After nucleation, these voids would grow and eventually coalesce where a crack forms and the material fractures[7].

Typically, uniform void growth is observed. However, for the alloys with a mixture of hard/soft matrix, non-uniform void growth is observed. This phenomenon is also observed during void nucleation where the different inclusion sizes can influence the void formation. The interaction of different void sizes can result in different growth rates which eventually lead to the fact that bigger sized voids outgrow the smaller ones[8, 9]. Through this paper, the event of non-uniform void growth will be regarded as bimodal voids.

A study done by Melander and Stahlberg involves mathematical models to test out the different relationships between bimodal voids sizes and populations with the ductility of the material. Several conclusions were made from the study[10]:

1. Bimodal distribution of voids are more ductile compared to uniform ones as the bimodal voids must be strained further
2. Ductility increases as the distance between the two different sized voids increase in a matrix
3. Smaller voids in a matrix have little influence on the overall ductility of the material unless the small voids have a similar or greater density than the larger voids in the material
4. Higher width to height ratios (or minor/major void lengths) increases the ductility but can be altered depending on the volume fraction of the voids distributed in the matrix

METHODS AND MATERIALS

The materials used in this work are laboratory-cast ingots and continuous casted slabs. Raw materials were melted in an induction furnace under vacuum and the ingots were top-poured. The representative compositions (in wt.%) of the ingots are shown in **Table 1**. As shown in **Figure 1(a)**, the steel ingots were cast in a 30 cm x 30.5 cm x 18 cm top pour mold and further sectioning of the ingots is as indicated in **Figure 1(b)**. The aim of the laboratory-cast ingots was to simulate the conditions of the continuous casted slabs. The chemical composition range of the continuous casted slabs are also within the same range of the compositions for the ingots shown below. Specifically, Slab A and Slab B have similar compositions to the listed compositions below.

Table 1. Chemical compositions of all as-cast AHSSs ingots with constant 2.5 wt% Mn.

Mn Group	Steel Name	C (wt. %)	Mn (wt. %)	Si (wt. %)	Al (wt. %)	Fe (wt. %)
2.5 Mn	1 Si 1 Al	0.19	2.52	1.02	1.05	Bal.
	1.5 Si 1.5 Al	0.19	2.52	1.55	1.52	Bal.

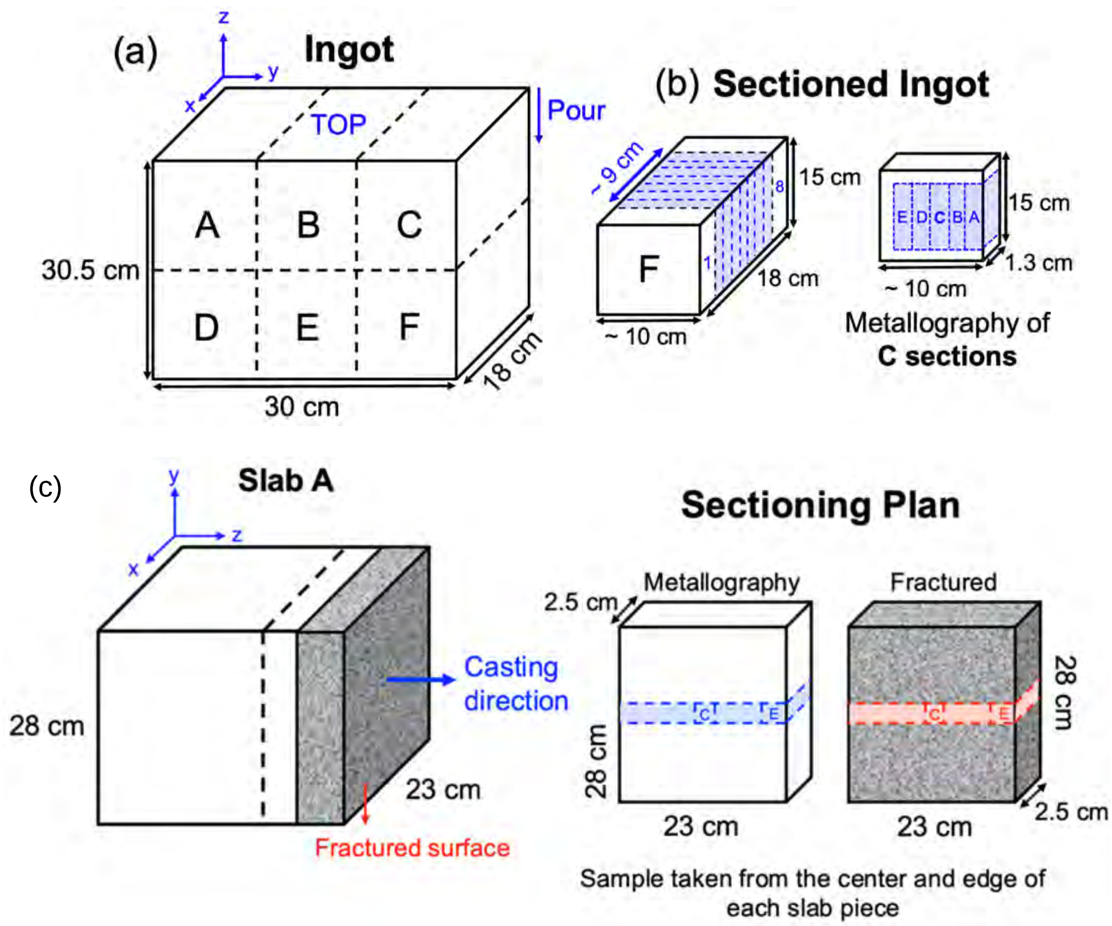

Figure 1. Ingot dimensions and steel cut schematic showing (a) 30 cm x 30.5 cm x 18 cm ingot cast dimensions, (b) F ingot slab cut where individual slabs are sectioned about into 5 sections (A through E) in which metallography is done at the center C section and (c) the dimensions of the slabs as received and the slab sectioning plan.

Metallographic sections in the z-direction (**Figure 1**) of the ingots were prepared and was first etched with 5% Nital and then further etched with 1.3% saturated Picric acid (in aqueous solution). Samples were etched for 5-20 seconds depending on the composition by immersion in the etchant. All samples were imaged and characterized using the light optical microscope Zeiss Axio Imager.Z2 Vario and were also observed under SEM using the Tescan MIRA. All ferrite quantifications were carried out using Sci-kit segmentation codes[4] for primary ferrite segmentation. For proeutectoid ferrite segmentation, the segmentation was done primarily through ImageJ. Uncertainties from the ferrite percentages are determined by the T-test.

To compare the ferrite percentages observed experimentally, Thermo-Calc diffusion simulations were carried out using the cooling rate approximated from QuikCast simulations (0.35ºC/sec) and Thermo-Calc 2024a version. The databases used for the simulation were TCFE-13.1 and MOBFE8.1 and the compositions for these simulations were narrowed to Fe-C-Mn-Si-Al.

Hardness tests were performed using the Wilson VH3300 Automatic Tester. Tensile specimens were cut and machined from the ingots using sections A, B, D and E (schematic shown in **Figure 1** above). The samples were round threaded 10 mm tensile bar specimens with a reduced section of 6 mm diameter by 6 mm length center and a schematic of the sample is shown below in **Figure 2**.

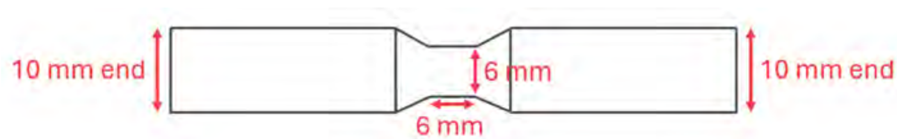

Figure 2. The schematic of Gleeble specimen showing a round threaded 10 mm end tensile bar with a reduced section of 6 mm diameter by 6 mm length center.

© 2025 by the Association for Iron & Steel Technology.

All samples were tested using the Gleeble 3500-GTC machine. All tensile tests were carried out at 200ºC, 400ºC and 600ºC with at least 3 samples per temperature. All samples were welded with a K-type thermocouple to monitor the temperature during the tests. After all tensile tests, each sample was cut down using a low-speed saw, and the fracture surfaces were reassembled and cross-sectioned to view the fracture path (shown in **Figure 3**).

Figure 3. Schematic of fractured specimens were reassembled for cross-section after fracture.

RESULTS AND DISCUSSION

Microstructure Analysis

Initially, the as-cast microstructures of all ingots and the fractured continuous casted specimens were observed by looking at the metallographic cross-sections. Through observations from **Figure 4**, there are different ferrite morphologies depending on the chemical compositions. From the images, some common morphologies can be identified. Proeutectoid ferrite is seen in individual Si-alloyed group, low addition Si + Al (images not shown) for both 2.5 Mn and Slab B. Primary ferrite is observed in individual Al-alloyed steels, most high addition Si + Al alloys for 2.5 Mn and Slab A.

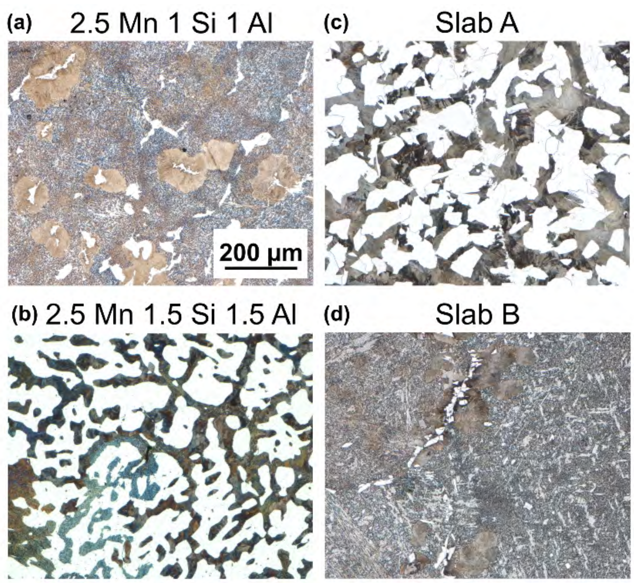

Figure 4. Light optical microscopy images for representative groups of ingots and slabs: (a) 2.5 Mn 1 Si 1 Al, (b) 2.5 Mn 1.5 Si 1.5 Al, (c) Slab A and (d) Slab B.

From the optical images, the amounts of ferrite were quantified for all ingots and slabs and are summarized in **Figure 5** below. Comparing the amounts of ferrites, individual Si-alloyed steels and Slab B have the lowest ferrite percentages. However, as the Si and Al additions increase in the steel, the ferrite amounts increased up to 40% in the Si + Al steels as both Si and Al are strong ferrite stabilizers which can promote the formation of ferrite. The ferrite percentage found in 2.5 Mn 1.5 Si 1.5 Al is comparable to the amount found in Slab A where it is shown to have similar ferrite percentages. However, since Slab A and B have similar compositions, both are expected to have similar ferrite morphologies and amounts and so the difference suggests the steels might have cooled differently for both slabs.

© 2025 by the Association for Iron & Steel Technology.

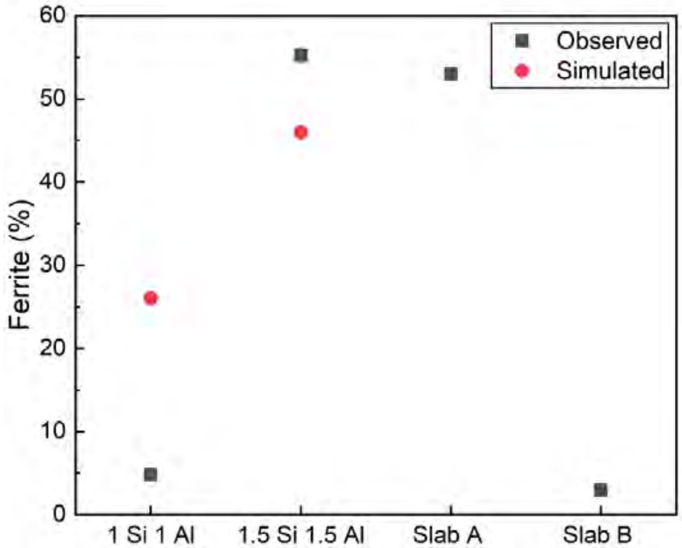

Figure 5. Ferrite percentages for all compositions (ingots and slabs) comparing experimental observations with Thermo-Calc diffusion simulation results.

While it was apparent that the ferrite morphologies differ among the compositions, it was unclear on whether the other microstructure are the same. To investigate, SEM imaging of all the compositions were done to investigate the second microstructure. The images are as shown below in **Figure 7**.

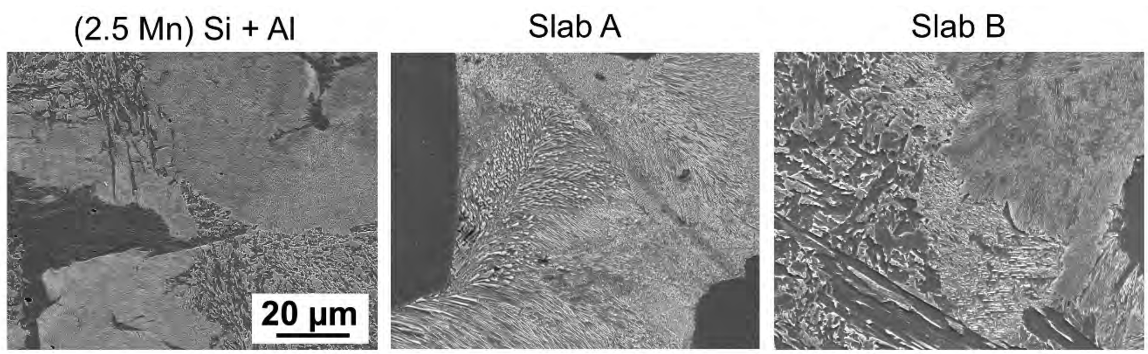

Figure 6. SEM images for all chemical composition groups for ingots and slabs.

From the SEM images, there are two different microstructures identified. The 2.5 Mn ingot group with Si + Al and Slab B have bainite, pearlite and ferrite in the microstructure as the pearlite has finer lamellar spacings compared to the thicker bainitic laths. On the contrary, only Slab A contains pearlite and ferrite. The difference in this microstructure suggests a difference in the cooling rates between the ingots and slabs.

The difference in cooling rates between Slab A and Slab B could have also explained the difference in the ferrite amounts seen. According to Chen et. al[11], increasing the cooling rate gradually changes the microstructure and that the amount of ferrite decreases. This is due to the increase in austenite transforming to pearlite instead of ferrite which can also be dependent on the transformation temperature during the casting process. Hence, it is why it is observed that there are more ferrite seen in Slab A than Slab B as Slab A cooled slower than Slab B.

Mechanical Properties
The difference in the microstructures indicated that there can be a difference in the mechanical properties between the as-cast ingots and continuous casted slabs. This difference is shown in **Figure 7** where the hardness test for all samples is summarized. From the comparison plot, the ingots have higher hardness than the slabs and 1 Si 1 Al have the highest hardness overall. Slab B and 1.5 Si 1.5 Al have comparable hardness while Slab A has the lowest hardness among the four compositions. Since Slab A has much higher ferrite amount than Slab B, it is expected to have a lower hardness, and this is depicted in the figure. However, this suggests that since Slab A has a lower hardness than Slab B, it has a higher impact toughness and therefore may have a different cracking mechanism than Slab B.

© 2025 by the Association for Iron & Steel Technology.

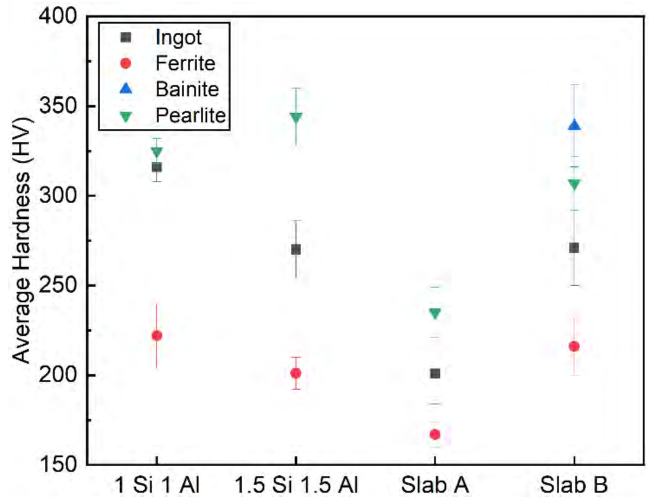

Figure 7. Average ingot, ferrite, bainite and pearlite (HV) with their respective uncertainties for all ingots grouped according to their total additions and all slabs.

From the force-displacement curves tested for all compositions, the yield strengths are approximated for all ingots and slabs (in **Figure 8**). Across all slabs and ingots, 1 Si 1 Al has the highest strength for the ingots and Slab B has the highest strength for the slab. For all ingots and slabs, the highest yield strength peaks at 400ºC. While the full mechanism of why this could have happened is not fully understood, it can be suggested that at this temperature the C tendency to pin dislocations increases which increases the yield strength of the steel as compared to 200ºC.

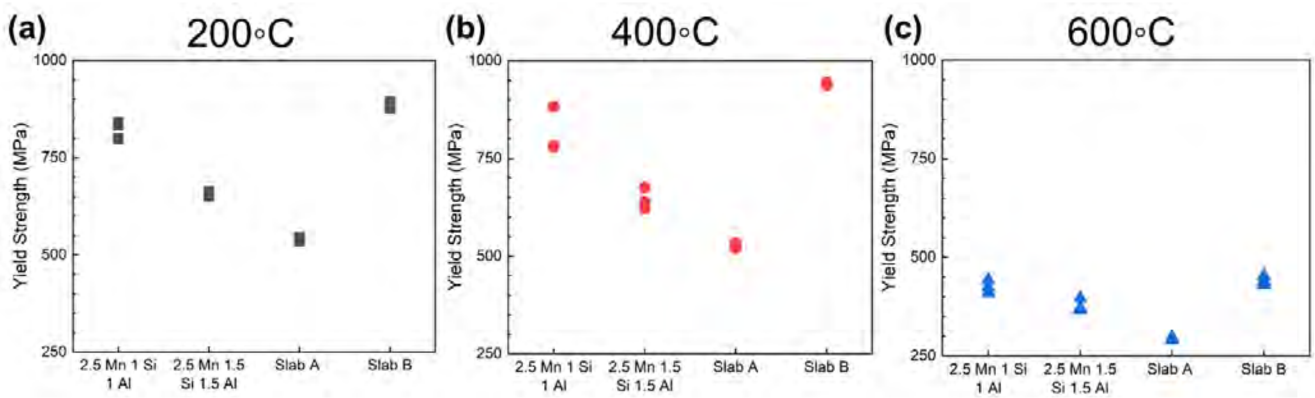

Figure 8. Approximate yield strength (MPa) for all slabs and ingots at 200ºC, 400ºC and 600ºC grouped according to the total addition, Mn group and slab.

The reduction in area was measured for all compositions and is summarized below in **Figure 9** for temperatures 200ºC, 400ºC and 600ºC. Overall, the reduction in area is high and within the same range for 2.5 Mn ingots where the reduction in area is comparable and within the same range for the three tested temperatures. Comparing Slab A to Slab B, the reduction in area for Slab B is lower than the reduction in area for Slab A. The ductility observed in Slab A is as comparable to the reduction in area for 2.5 Mn ingots. With the high yield strength observed for Slab B, it is expected that the ductility will be lower.

© 2025 by the Association for Iron & Steel Technology.

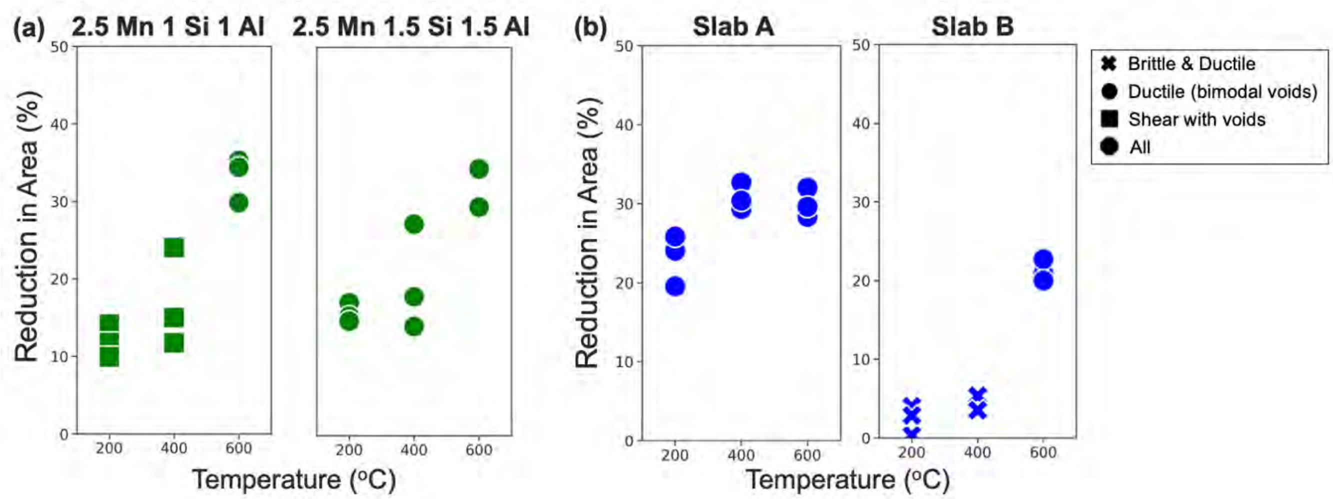

Figure 9. Reduction in area (%) vs. Temperature (°C) for all four compositions with the different colors for different groups of steels (green = 2.5 Mn ingots and blue = slabs) and the labels for the type of fracture occurred for each sample at each temperature.

CONCLUSIONS

In this study, comparisons between the microstructures and mechanical properties of all compositions between ingots and slabs were done. From the results shown above, some conclusions could be deduced:

1. There are two ferrite morphologies – primary and proeutectoid ferrite and the morphology depends on the element addition in the steels.
2. As the total addition increases, the ferrite amounts also increase in the ingots. This is not applicable for the slabs as the slabs have similar concentration and addition amounts which suggests the cooling profile is different for the two slabs.
3. There are two different microstructures identified for all ingots and slabs: pearlite + bainite + ferrite (seen in 2.5 Mn 1 Si 1 Al and Slab B) and pearlite + ferrite (Slab A and 2.5 Mn 1.5 Si 1.5 Al).
4. Hardness is highest for 1 Si 1 Al. Comparing the two slabs, Slab A overall has lower ductility, hardness and strengths compared to Slab B which relates to their microstructure as Slab B has pearlite + bainite + ferrite in its microstructure.
5. For Slab A and 2.5 Mn ingots, these compositions exhibit the highest ductility. While Slab A is not as comparable to the ingots, it has the higher ductility when compared to Slab B.

ACKNOWLEDGEMENTS

The author acknowledges the financial support from the Center of Iron and Steel Research at Carnegie Mellon University and the use of the Materials Characterization Facility at Carnegie Mellon University supported by grant MCF-677785.

REFERENCES

1. R. Kuziak, R. Kawalla, and S. Waengler, “Advanced high strength steels for automotive industry,” Archives of Civil and Mechanical Engineering, vol. 8, no. 2, pp. 103–117, (2008) doi: 10.1016/S1644-9665(12)60197-6.
2. Automotive Steels. Elsevier, 2017. doi: 10.1016/C2015-0-00236-2.
3. A. K. Perka, M. John, U. B. Kuruveri, and P. L. Menezes, “Advanced High-Strength Steels for Automotive Applications: Arc and Laser Welding Process, Properties, and Challenges,” Metals, vol. 12, no. 6, p. 1051, Jun. 2022, doi: 10.3390/met12061051.
4. S. van der Walt et al., “scikit-image: image processing in Python,” PeerJ, vol. 2, p. e453, Jun. 2014, doi: 10.7717/peerj.453.
5. J. Chen, G. Feng, Y. Zheng, P. Lin, L. Wang, and Y. Li, “Effect of Cooling Rate on Microstructure Evolution and Mechanical Properties of SCM435 Steel,” Metals, vol. 14, no. 2, p. 140, Jan. 2024, doi: 10.3390/met14020140.
6. Pineau, A., A.A. Benzerga, and T. Pardoen. “Failure of Metals I: Brittle and Ductile Fracture.” Acta Materialia 107 (April 2016): 424–83. https://doi.org/10.1016/j.actamat.2015.12.034.

© 2025 by the Association for Iron & Steel Technology.

7. Pineau, A., and T. Pardoen. “Failure of Metals.” In Comprehensive Structural Integrity, 321–432. Elsevier, 2003. https://doi.org/10.1016/B978-0-12-822944-6.00135-3.
8. Tvergaard, Viggo. “Interaction of Very Small Voids with Larger Voids.” International Journal of Solids and Structures 35, no. 30 (October 1998): 3989–4000. https://doi.org/10.1016/S0020-7683(97)00254-0.
9. Tvergaard, V., and A. Needleman. “Effect of Crack Meandering on Dynamic, Ductile Fracture.” Journal of the Mechanics and Physics of Solids 40, no. 2 (January 1992): 447–71. https://doi.org/10.1016/S0022-5096(05)80021-3.
10. A. Melander and U. Stahlberg, “The effect of void size and distribution on ductile fracture,” Int J Fract, vol. 16, no. 5, pp. 431–440, Oct. 1980, doi: 10.1007/BF00016582.
11. J. Chen, G. Feng, Y. Zheng, P. Lin, L. Wang, and Y. Li, “Effect of Cooling Rate on Microstructure Evolution and Mechanical Properties of SCM435 Steel,” Metals, vol. 14, no. 2, p. 140, Jan. 2024, doi: 10.3390/met14020140.
12. Dieter, George E. Mechanical Metallurgy. 3rd ed. McGraw-Hill Series in Materials Science and Engineering. New York: McGraw-Hill, 1986.

© 2025 by the Association for Iron & Steel Technology.